



Nitrous oxide emissions 1999 to 2009 from a global atmospheric inversion

R. L. Thompson¹, F. Chevallier², A. M. Crowell^{3,11}, G. Dutton³, R. L. Langenfelds⁴, R. G. Prinn⁵, R. F. Weiss⁶, Y. Tohjima⁷, T. Nakazawa⁸, P. B. Krummel⁴, L. P. Steele⁴, P. Fraser⁴, S. O'Doherty⁹, K. Ishijima¹⁰, and S. Aoki⁹

¹Norwegian Institute for Air Research, Kjeller, Norway

²Laboratoire des Sciences du Climat et de l'Environnement, Gif sur Yvette, France

³NOAA ESRL, Global Monitoring Division, Boulder, CO, USA

⁴Commonwealth Scientific and Industrial Research Organisation, Aspendale, Australia

⁵Center for Global Change Science, MIT, Cambridge, MA, USA

⁶Scripps Institution of Oceanography, La Jolla, CA, USA

⁷National Institute for Environmental Studies, Tsukuba, Japan

⁸Center for Atmospheric and Oceanic Studies, Graduate School of Science, Tohoku University, Sendai 980-8578, Japan

⁹Atmospheric Chemistry Research Group, School of Chemistry, University of Bristol, Bristol, UK

¹⁰Japan Agency for Marine-Earth Science and Technology, Yokohama, Japan

¹¹Cooperative Institute for Research in Environmental Sciences, University of Colorado, Boulder, CO, USA

Correspondence to: R. L. Thompson (rona.thompson@nilu.no)

Received: 22 March 2013 – Published in Atmos. Chem. Phys. Discuss.: 13 June 2013

Revised: 8 January 2014 – Accepted: 9 January 2014 – Published: 17 February 2014

Abstract. N₂O surface fluxes were estimated for 1999 to 2009 using a time-dependent Bayesian inversion technique. Observations were drawn from 5 different networks, incorporating 59 surface sites and a number of ship-based measurement series. To avoid biases in the inverted fluxes, the data were adjusted to a common scale and scale offsets were included in the optimization problem. The fluxes were calculated at the same resolution as the transport model (3.75° longitude × 2.5° latitude) and at monthly time resolution. Over the 11-year period, the global total N₂O source varied from 17.5 to 20.1 Tg a⁻¹ N. Tropical and subtropical land regions were found to consistently have the highest N₂O emissions, in particular in South Asia (20 ± 3 % of global total), South America (13 ± 4 %) and Africa (19 ± 3 %), while emissions from temperate regions were smaller: Europe (6 ± 1 %) and North America (7 ± 2 %). A significant multi-annual trend in N₂O emissions (0.045 Tg a⁻² N) from South Asia was found and confirms inventory estimates of this trend. Considerable interannual variability in the global N₂O source was observed (0.8 Tg a⁻¹ N, 1 standard deviation, SD) and was largely driven by variability in tropical and subtropical soil fluxes, in particular in South America (0.3 Tg a⁻¹ N, 1 SD)

and Africa (0.3 Tg a⁻¹ N, 1 SD). Notable variability was also found for N₂O fluxes in the tropical and southern oceans (0.15 and 0.2 Tg a⁻¹ N, 1 SD, respectively). Interannual variability in the N₂O source shows some correlation with the El Niño–Southern Oscillation (ENSO), where El Niño conditions are associated with lower N₂O fluxes from soils and from the ocean and vice versa for La Niña conditions.

1 Introduction

Nitrous oxide (N₂O) is now the third largest contributor to anthropogenic radiative forcing among the long-lived greenhouse gases (GHGs) and has a global warming potential of approximately 300 times that of CO₂ (Forster et al., 2007). N₂O also plays an important role in stratospheric ozone depletion through the formation of NO and, with the decrease in chlorofluorocarbon (CFC) emissions, is the dominant ozone-depleting substance currently emitted (Ravishankara et al., 2009). Emissions of N₂O have been increasing since the pre-industrial era due to human activities, leading to substantial increases in the atmospheric mole fraction, from

270 nmol mol⁻¹ (abbreviated as ppb; 1 nmol = 10⁻⁹ mol) to around 323 ppb today (WMO, 2011). N₂O emissions occur naturally as a byproduct of the processes of denitrification (microbial reduction of nitrate and nitrite) and nitrification (microbial oxidation of ammonia), which occur in soils and in the ocean. Several human activities enhance nitrification and denitrification rates and, consequently, emissions of N₂O to the atmosphere. The most significant of these activities is food production through the use of nitrogen fertilizers, manure, and land cultivation (Syakila and Kroeze, 2011), with smaller contributions from bio-fuel production (Crutzen et al., 2008). There are also direct N₂O emissions from industry, combustion and municipal waste (Denman et al., 2007).

Atmospheric monitoring of N₂O started in the late 1970s and has been instrumental in determining long-term emission trends (Syakila and Kroeze, 2011), and more recently with improved data precision, in determining the spatial distribution of emissions (Hirsch et al., 2006; Huang et al., 2008). Superimposed on the long-term trend in atmospheric N₂O, is considerable interannual variability in the growth rate. To date, there have been only a few studies that have tried to understand the mechanisms driving this variability (Nevison et al., 2007, 2011; Thompson et al., 2013). On the one hand, the growth rate is influenced by changes in non-emission related variables, such as atmospheric transport, especially stratosphere-to-troposphere transport, which carries N₂O-depleted air from the stratosphere into the troposphere and has a significant influence on the observed N₂O seasonal cycle and also contributes to interannual variability (Nevison et al., 2011). On the other hand, it is known from in situ flux measurements that terrestrial biosphere fluxes of N₂O are strongly determined by climatological factors such as soil temperature, moisture and precipitation (Bouwman et al., 2002; Skiba and Smith, 2000; Smith et al., 1998). A number of land ecosystem models now include the nitrogen cycle and simulate N₂O fluxes (Potter et al., 1996; Zaehle et al., 2010), but owing to the non-linear response of N₂O production to soil and climate parameters, as well as to nitrogen substrate availability, the modelled fluxes are associated with large uncertainties (Werner et al., 2007). Some ecosystem models predict a significant N₂O soil-flux–climate link. In a study by Xu et al. (2012) the sensitivity of N₂O emissions to soil temperature was found to be 1 Tg of N equivalents of N₂O (abbreviated Tg N) per kelvin per year. A study by Zaehle et al. (2011) also found a strong link between N₂O soil emissions and climate. It has not been possible, however, to verify modelled interannual variability in the N₂O flux, since sufficient long-term in situ flux measurements are not available. Therefore, to learn more about interannual variability in N₂O fluxes, and especially the integrated response at regional or continental scales of N₂O flux to climate forcing, it is useful to turn to atmospheric observations.

Numerous multi-annual flux studies have been carried out for the other important GHGs, CO₂ (Bousquet et al., 2000; Rayner et al., 1999; Rödenbeck et al., 2003) and CH₄

(Bousquet et al., 2006; Chen and Prinn, 2006), using atmospheric observations and the inversion of atmospheric transport. These flux studies found the land–atmosphere fluxes of both these species to be significantly sensitive to climate variability and in particular to the El Niño–Southern Oscillation (ENSO) climate variation and to the climate impacts of the Pinatubo eruption (Bousquet et al., 2006; Chen and Prinn, 2006; Peylin et al., 2005; Rödenbeck et al., 2003). To the best of our knowledge, no previous multi-annual inversion study of this type has been conducted for N₂O. In this study, we focus on N₂O fluxes from 1999 to 2009, since the data precision improved greatly during the 1990s and since a number of new sites became operational in the late 1990s and early 2000s. The inversions were run from 1996 to 2009, but we only examine the data from 1999 since the first 3 years of simulation were needed for spin-up. (The long spin-up time was required to achieve realistic tropospheric and stratospheric mole fractions, which depend on the surface source, the stratospheric sink and the rate of air mass exchange across the tropopause.)

In this paper, we first describe the inversion method and atmospheric transport model used, as well as provide details on the atmospheric observations that were included (Sect. 2). Second, we describe a number of tests that were performed for the sensitivity of the observation network to changes in N₂O emissions and for the sensitivity of the inversions to their prior emission estimates (Sects. 2.6 and 2.7, respectively). In Sects. 3 and 4, we discuss the results of the inversions and the variability and trends in the retrieved N₂O emissions.

2 Inversion method

2.1 Bayesian inversion

In this study, we used a Bayesian inversion method to find the optimal surface fluxes at monthly temporal resolution and at the same spatial resolution as the atmospheric transport model (i.e. 3.75° × 2.5° longitude by latitude). The inversion is performed in two time intervals: from 1996 to 2003 and 2002 to 2009. The first 3 years of the first period and the first 2 years of the second period were used for spin-up. (A 2-year spin-up time was considered sufficient for the second period, since the initial conditions for 2002 from the first period were reused in the second period). According to the Bayesian method, the optimal solution (in this study, the surface fluxes and the initial mole fractions), \mathbf{x} , is that which provides the best fit to the atmospheric observations, \mathbf{y} , while remaining within the bounds of the prior estimates, \mathbf{x}_b , and their uncertainties (for details about the Bayesian method refer to Tarantola, 2002). The extra constraint of the prior prevents the problem from being ill-conditioned in the mathematical sense. Based on Bayesian theory, as well as Gaussian-error

hypotheses, one can derive the following cost function:

$$J(\mathbf{x}) = (\mathbf{x} - \mathbf{x}_b)^T \mathbf{B}^{-1} (\mathbf{x} - \mathbf{x}_b) + (H(\mathbf{x}) - \mathbf{y})^T \mathbf{R}^{-1} (H(\mathbf{x}) - \mathbf{y}) \quad (1)$$

where the flux uncertainties are described by the error covariance matrix, \mathbf{B} ; the observation uncertainties are described by the error covariance matrix, \mathbf{R} ; and H is a non-linear operator for atmospheric transport and chemistry (in Eq. 1, the matrix transpose is indicated by T). To solve this equation, we used the variational framework of Chevallier et al. (2005). In this approach, the minimum of $J(\mathbf{x})$ is found iteratively using a descent algorithm based on the Lanczos version of the conjugate gradient algorithm (Lanczos, 1950). This algorithm requires several computations of the gradient of J with respect to \mathbf{x} (where \mathbf{H} is the linearized form of the transport operator, H):

$$\nabla J(\mathbf{x}) = \mathbf{B}^{-1} (\mathbf{x} - \mathbf{x}_b) + \mathbf{H}^T \mathbf{R}^{-1} (H(\mathbf{x}) - \mathbf{y}). \quad (2)$$

For problems with a very large number of variables, it is not possible to directly define \mathbf{H} or \mathbf{H}^T owing to numerical limitations. Therefore, the elements of \mathbf{H}^T are found implicitly via the adjoint model of the atmospheric transport and chemistry (Chevallier et al., 2005; Errico, 1997).

2.2 Transport model

The inversion framework relies on the offline version of the Laboratoire de Météorologie Dynamique version 4 (LMDz) general circulation model (Hourdin and Armengaud, 1999; Hourdin et al., 2006). This version computes the evolution of atmospheric compounds using archived fields of winds, convection mass fluxes and planetary boundary layer (PBL) exchange coefficients that have been built from prior integrations of the complete general circulation model, which was nudged to ECMWF ERA-Interim winds (Uppala et al., 2005). The LMDz model is on a 3-D Eulerian grid consisting of 96 zonal columns, 73 meridional rows and 19 hybrid pressure levels. The daytime PBL is resolved by 4–5 levels, the first of which corresponds to 70 m altitude and the other levels spaced between 300 and 500 m apart from there on upwards. Above the PBL the mean resolution is 2 km up to a height of 20 km, above which there are four levels with the uppermost level at 3 hPa. Tracer transport is calculated in LMDz using the second-order finite-volume method of Van Leer (1977) and is described for LMDz by Hourdin and Armengaud (1999). Turbulent mixing in the PBL is parameterized using the scheme of Mellor and Yamada (1982) and thermal convection is parameterized according to the scheme of Tiedtke et al. (1989). The offline LMDz was run with a physical time step of 30 min. For the calculation of J and its gradient ∇J (Eqs. 1 and 2), the tangent linear \mathbf{H} and adjoint \mathbf{H}^T operators were coded from the offline LMDz version (Chevallier et al., 2005).

In the case of N_2O , the sink in the stratosphere needs to be accounted for. Losses of N_2O occur via photolysis and reac-

tion with $\text{O}(^1\text{D})$ accounting for 90 % and 10 % of the sink, respectively (Minschwaner et al., 1993). These reactions were included in the forward and adjoint models of the atmospheric transport as described in Thompson et al. (2011). The number density of $\text{O}(^1\text{D})$ and the photolysis rate were defined for each grid cell and time step and were taken from prior simulations of the coupled global circulation and atmospheric chemistry model LMDz-INCA (Hauglustaine et al., 2004) with the same transport fields as used in the inversion. The fields of photolysis rate from LMDz-INCA were scaled by a factor of 0.66 to give a mean total annual loss of N_2O of $12.2 \text{ Tg a}^{-1} \text{ N}$, consistent with estimates of N_2O lifetime between 124 and 130 years (Prather et al., 2012; Volk et al., 1997). This was necessary as the fields from LMDz-INCA had not been previously optimized for use in N_2O inversions, and without this scaling the lifetime would have been circa 84 years.

2.3 Prior flux estimates

Our a priori N_2O flux estimate (\mathbf{x}_b in Eqs. 1 and 2) was compiled from different models/inventories for

- terrestrial biosphere fluxes, including natural and cultivated ecosystems;
- anthropogenic emissions, from fossil and bio-fuel combustion, industry, and municipal waste;
- biomass burning emissions;
- coastal and open ocean fluxes.

The terrestrial biosphere fluxes were provided from the nitrogen version of the ORCHIDEE land surface model (O-CN, version 0.74, Zaehle and Friend, 2010). O-CN accounts for nitrogen input from atmospheric deposition, biological nitrogen fixation and fertilizer usage and simulates nitrogen losses via leaching, nitrification and denitrification pathways, and emissions of trace gases to the atmosphere. The model is driven by climate data (CRU-NCEP) and interannually varying N inputs. Data were originally provided at $3.75^\circ \times 2.5^\circ$ (longitude by latitude) and monthly resolution. For the anthropogenic emissions (excluding direct agricultural emissions, which are accounted for in O-CN), we used EDGAR-4.1 (Emission Database for Global Atmospheric Research) inventory data. These data were provided at $1.0^\circ \times 1.0^\circ$ and annual resolution. Since N_2O emissions from these sources are small relative to the terrestrial biosphere and ocean sources, and because they have relatively little seasonality, annual resolution is considered sufficient. The biomass burning emissions were provided by the Global Fire Emissions Database (GFED-2.1) at $1.0^\circ \times 1.0^\circ$ and monthly resolution (van der Werf et al., 2010). For the ocean fluxes, we used estimates provided by the ocean biogeochemistry model PISCES, which was embedded in a climate model but was not constrained by meteorological data; thus interannual

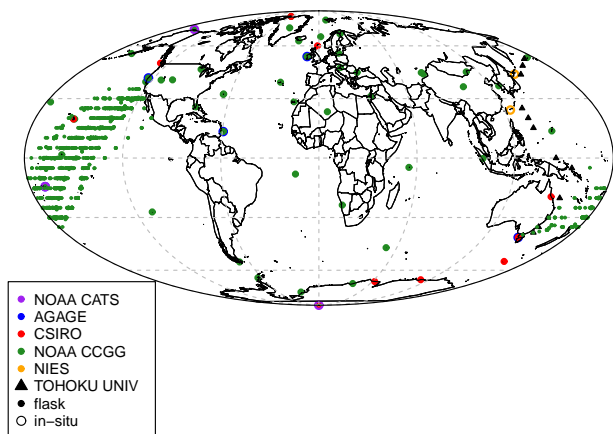


Fig. 1. Map of observation sites and ship tracks by network.



Fig. 2. N_2O observation availability at individual sites for the inversion period 1999 to 2009. The legend indicates the number of observations per month.

variations may not be in phase with observations (Dutreuil et al., 2009). Data were provided at $1.0^\circ \times 1.0^\circ$ and monthly resolution. (See Table 3 for the global N_2O emission from each source.)

2.4 Observations

Atmospheric observations were pooled from a number of global networks, independent sites and ship-based measurements (see Figs. 1 and 2 and Table 1). Long-term records of N_2O mole fraction are available from the Advanced Global Atmospheric Gases Experiment (AGAGE, http://cdiac.ornl.gov/ftp/ale_gage_Agage/AGAGE/) and the NOAA Halocarbons and other Atmospheric Trace Species (HATS, <http://www.esrl.noaa.gov/gmd/hats/>), including both the OTTO and the Chromatograph for Atmospheric Trace Species (CATS, <http://www.esrl.noaa.gov/gmd/hats/insitu/cats/>) programmes, which were established in the 1990s. The early data, however, cannot be used to constrain regional fluxes of N_2O owing to the less precise instrumentation available at that time. During the 1990s significant improvements to the measurement technique were made and, thus, sufficiently precise data from these networks are available from the mid-to late 1990s. Both the AGAGE and CATS networks consist of stations equipped with in situ gas chromatographs with electron capture detectors (GC-ECD) to measure the dry air mole fraction of N_2O (ppb) and provide measurements at approximately 40 min intervals. The AGAGE data are reported on the SIO1998 scale and have an uncertainty on individual measurements of about 0.1 ppb (Prinn et al., 2000), while the NOAA CATS data are reported on the NOAA2006 scale and have an uncertainty of about 0.3 ppb (Hall et al., 2007). In the late 1990s and early 2000s, NOAA also established a flask network under the Carbon Cycle and Greenhouse Gases (CCGG, <http://www.esrl.noaa.gov/gmd/ccgg/>) programme. Flask samples from this network are also analysed by GC-ECD in a central laboratory and are reported on the NOAA2006A scale. These data have an uncertainty of 0.4 ppb based on the mean value of differences from paired flasks. There is some concern that there could be a calibration shift between NOAA CCGG data collected before and after 2001, owing to a poor calibration routine used prior to 2001. To test for the influence of this shift on the retrieved fluxes, we include an inversion test in which minimal NOAA CCGG data are included (test IAVR; see section 2.7 for details). The Commonwealth Scientific and Industrial Research Organisation (CSIRO) in Australia have also operated a flask network since the early 1990s (data available from the World Data Centre for Greenhouse Gases, <http://ds.data.jma.go.jp/gmd/wdccc/>). These measurements are reported on the NOAA2006 scale with an uncertainty of approximately 0.3 ppb for each flask measurement (Francey et al., 2003). In addition, we included data from two stations operated by the National Institute for Environmental Science (NIES) in Japan, which operate in situ GC-ECDs (Tohjima et al., 2000) (data available from the World Data Centre for Greenhouse Gases, <http://ds.data.jma.go.jp/gmd/wdccc/>). These data are reported on NIES's own scale, which is approximately 0.6 ppb lower than NOAA2006A for ambient concentrations as determined from an intercomparison of

NOAA standards (see <http://www.esrl.noaa.gov/gmd/ccgg/wmorrr/results.php?rr=rr5¶m=n2o>). Lastly, we include data from ship-based flask measurements in a programme operated by Tohoku University, Japan (data available from the World Data Centre for Greenhouse Gases, <http://ds.data.jma.go.jp/gmd/wdogg/>) (Ishijima et al., 2009). Comparisons with NOAA standards indicate that the Tohoku measurements are approximately 0.2 ppb higher than the NOAA2006A scale. (For a list of all stations and their locations, see Table 1.)

Gradients of N₂O mole fraction in the atmosphere, which provide information about the distribution of N₂O fluxes, can be small and of the same order of magnitude as the calibration offsets between different scales and networks. For this reason, it is of critical importance to correct for these offsets prior to and/or in the inversion. Corazza et al. (2011) incorporated the optimization of calibration offsets into their inversion problem, thereby reducing the bias that these have on the retrieved fluxes. We adopt the same approach as Corazza et al. (2011), but, in addition, we corrected the observations based on our prior estimated calibration offsets before running the inversion. Using both approaches means that the inversion will only “fine-tune” the offsets, thereby limiting the degrees of freedom that can be used for this adjustment. Prior calibration offsets were estimated relative to NOAA CCGG (NOAA2006A scale) based on the comparison of observations from two or more networks at the same location, e.g. in American Samoa, where NOAA CATS, NOAA CCGG and AGAGE all have measurements. Overlaps between NOAA CCGG and AGAGE also exist at MHD, CGO, RPB and THD, as well as between NOAA CCGG and CSIRO at ALT, MLO, CGO and SPO, where the data were corrected to the NOAA2006A scale using the linear trend and offset calculated at each site (see Table 2). At sites where there was no overlap, the mean of the corrections applied to other sites within the same network was used. For NIES, which has no overlap with other networks, a temporally fixed offset was used and was based on shared cylinder intercomparisons with NOAA CCGG (Y. Tohjima, personal communication, 2012). The comparisons of AGAGE and NOAA CCGG data show a significant trend in the offset (0.02–0.04 ppb a⁻¹), which is consistent at all compared sites and points to a possible calibration drift in the scales relative to each other. However, without further detailed investigation it is not possible to tell how much each scale may have drifted and in which direction, but this drift could be significant when considering N₂O emission trends.

All data were filtered for suspicious values using flags set by the data providers. Additionally, the data were filtered for outliers, which were defined as points outside 2 standard deviations (SD) of the running mean calculated over a window of 45 days for flask data and 3 days for in situ data. The window lengths were optimized on a trial basis to ensure that only suspicious values were removed.

Observations from sites with in situ GC-ECDs were selected for the afternoon (12:00 to 17:00) if they were low-

altitude sites (<1000 m a.s.l.) and for the night (00:00 to 06:00) if they were mountain sites (>1000 m a.s.l.). These data selection criteria were chosen to minimize the impact of boundary layer vertical transport errors in the model. In general, data were assimilated at hourly resolution. For flask data, no selection was applied and data were assimilated when available. For the ship-based data (from Tohoku University), one observation was assimilated per grid cell and time step, and where more than one observation was available, the values were averaged. This was done to avoid assimilating highly correlated observations (observation error correlations are not taken into account; see Sect. 2.5.2).

2.5 Specification of uncertainties

2.5.1 Prior flux error covariance matrix

A key aspect of the Bayesian inversion is the description of prior flux uncertainty. This uncertainty is described by the error covariance matrix, **B** (in Eqs. 1 and 2), in which the diagonal elements are the error variances in each grid cell and time step and the off-diagonal elements are the covariances. Unfortunately, there are insufficient observations of N₂O flux to be able to accurately determine the error variances and covariances. Therefore, a simple approach for this was used; that is, we calculated the variance of each land grid cell as the maximum flux for the year found in the eight surrounding grid cells plus the cell of interest. Choosing the maximum value from nine grid cells allows the inversion to change the small-scale spatial pattern of the fluxes. For ocean grid cells, the errors were adjusted to 100% of the flux in the given grid cell; this is different to the land approach to avoid overestimating the errors in ocean grid cells along coastlines. The errors calculated for land in the Southern Hemisphere were scaled by 0.66 owing to the weaker observational constraint in this hemisphere and to allow for greater reliance on the prior estimates. Both land and ocean errors were set to a maximum of 0.44 g m⁻² a⁻¹ N and minimum of 0.03 g m⁻² a⁻¹ N. In areas covered by sea ice, the error was reduced by a factor of 100. The covariance was calculated as an exponential decay with distance and time using correlation scale lengths of 500 km over land and 1000 km over ocean and 12 weeks, respectively. The correlation scale length of the errors in land fluxes depends strongly on the source; here we chose 500 km as an educated guess to represent the correlation of the errors in the spatially diffuse soil emission, which is the dominant source and is modulated by land use, soil type, moisture and temperature, as well as by the amount of nitrogen input. The choice of 12 weeks for the temporal correlation length was to represent the correlation of fluxes within a season on a sub-continental scale, while at the same time, flux time steps 12 months apart only have a correlation of 0.02, so the posterior fluxes will not be strongly dependent on the prior interannual variability. The whole error covariance matrix was then scaled so that its sum was

Table 1. Observation sites used in the inversions. Sites in bold type were included in the reference data set. (FM stands for flask measurement, CM for continuous measurement, and SM for ship-based flask measurement.)

Station	Network	Latitude	Longitude	Altitude (m)	Type	Description
ALT	CCGG	82.45° N	62.52° W	210	FM	Alert, Nunavut, Canada
ALT	CSIRO	82.45° N	62.52° W	210	FM	Alert, Nunavut, Canada
ASC	CCGG	7.92° S	14.42° W	54	FM	Ascension Island, UK
ASK	CCGG	23.18° N	5.42° E	2728	FM	Assekrem, Algeria
AZR	CCGG	38.77° N	27.38° W	40	FM	Terceira Island, Azores
BAL	CCGG	55.35° N	17.22° E	7	FM	Baltic Sea, Poland
BKT	CCGG	0.2° S	100.32° E	865	FM	Bukit Koto Tabang, Indonesia
BME	CCGG	32.37° N	64.65° W	30	FM	St. Davis Head, Bermuda
BMW	CCGG	32.27° N	64.88° W	30	FM	Tudor Hill, Bermuda
BRW	CCGG	71.32° N	156.6° W	11	FM	Barrow, Alaska, USA
BRW	CATS	71.32° N	156.6° W	11	CM	Barrow, Alaska, USA
BSC	CCGG	44.17° N	28.68° E	3	FM	Black Sea, Romania
CBA	CCGG	55.2° N	162.72° W	21	FM	Cold Bay, Alaska, USA
CFA	CSIRO	19.28° S	147.05° E	2	FM	Cape Ferguson, Australia
CGO	CCGG	40.68° S	144.68° E	164	FM	Cape Grim, Tasmania
CGO	AGAGE	40.68° S	144.68° E	164	CM	Cape Grim, Tasmania
CGO	CSIRO	40.68° S	144.68° E	164	FM	Cape Grim, Tasmania
CHR	CCGG	1.7° N	157.17° W	3	FM	Christmas Island, Kiribati
COI	NIES	43.15° N	145.5° E	45	CM	Cape Ochi-ishi, Japan
CRZ	CCGG	46.45° S	51.85° E	120	FM	Crozet Island, France
CYA	CSIRO	66.28° S	110.53° E	60	FM	Casey Station, Australia
EIC	CCGG	27.15° S	109.45° W	50	FM	Easter Island, Chile
ESP	CSIRO	49.38° N	126.55° W	39	FM	Estevan Point, Canada
GMI	CCGG	13.43° N	144.78° E	2	FM	Mariana Island, Guam
HAT	NIES	24.05° N	123.8° E	10	CM	Hateruma, Japan
HBA	CCGG	75.58° S	26.5° W	30	FM	Halley Station, Antarctica
HUN	CCGG	46.95° N	16.65° E	344	FM	Hegyhatsal, Hungary
ICE	CCGG	63.25° N	20.29° W	118	FM	Heimay, Iceland
IZO	CCGG	28.3° N	16.48° W	2360	FM	Tenerife, Canary Islands
KEY	CCGG	25.67° N	80.2° W	3	FM	Key Biscayne, Florida, USA
KUM	CCGG	19.52° N	154.82° W	3	FM	Cape Kumukahi, Hawaii
KZM	CCGG	43.25° N	77.88° E	2519	FM	Plateau Assy, Kazakhstan
KZD	CCGG	44.06° N	76.82° E	601	FM	Sary Taukum, Kazakhstan
LEF	CCGG	45.93° N	90.27° W	868	FM	Park Falls, Wisconsin, USA
MAA	CSIRO	67.62° S	62.87° E	32	FM	Mawson, Australia
MHD	AGAGE	53.33° N	9.9° W	25	CM	Mace Head, Ireland
MHD	CCGG	53.33° N	9.9° W	25	FM	Mace Head, Ireland
MID	CCGG	28.22° N	177.37° W	4	FM	Sand Island, Midway, USA
MLO	CCGG	19.53° N	155.58° W	3397	FM	Mauna Loa, Hawaii
MLO	CSIRO	19.53° N	155.58° W	3397	FM	Mauna Loa, Hawaii
MQA	CSIRO	54.48° S	158.97° E	12	FM	Macquarie Island, Australia
NMB	CCGG	23.58° S	15.03° E	456	FM	Gobabeb, Namibia
NWP	TOHOKU	–	–	–	SM	Northwest Pacific, Japan
NWR	CCGG	40.05° N	105.58° W	3526	FM	Niwot Ridge, CO, USA
PAL	CCGG	67.97° N	24.12° E	560	FM	Pallas, Finland
POC	CCGG	–	–	–	SM	Pacific Ocean Shipboard
PSA	CCGG	64.92° S	64° W	10	FM	Palmer Station, Antarctica
PTA	CCGG	38.95° N	123.73° W	55	FM	Point Arena, CA, USA
RPB	AGAGE	13.17° N	59.43° W	45	CM	Ragged Point, Barbados
RPB	CCGG	13.17° N	59.43° W	45	FM	Ragged Point, Barbados
SEY	CCGG	4.67° S	55.17° E	3	FM	Mahe Island, Seychelles
SHM	CCGG	52.72° N	174.1° E	40	FM	Shemya Island, Alaska
SIS	CSIRO	60.08° N	1.25° W	30	FM	Shetland Island, UK
SMO	AGAGE	14.25° S	170.57° W	42	CM	Tutuila, American Samoa
SMO	CCGG	14.25° S	170.57° W	42	FM	Tutuila, American Samoa
SMO	CATS	14.25° S	170.57° W	42	CM	Tutuila, American Samoa
SPO	CCGG	89.98° S	24.8° W	2810	FM	South Pole, Antarctica
SPO	CSIRO	89.98° S	24.8° W	2810	FM	South Pole, Antarctica
SPO	CATS	89.98° S	24.8° W	2810	CM	South Pole, Antarctica
STM	CCGG	66.0° N	2.0° E	7	FM	Ocean Station M, Norway
SUM	CCGG	72.58° N	38.48° W	3238	FM	Summit, Greenland
SYO	CCGG	69.0° S	39.58° E	11	FM	Syowa Station, Antarctica
TAP	CCGG	36.73° N	126.13° E	20	FM	Tae-ahn Peninsula, Korea
TDF	CCGG	54.87° S	68.48° W	20	FM	Tierra del Fuego, Argentina
THD	AGAGE	41.05° N	124.15° W	107	CM	Trinidad Head, CA, USA
THD	CCGG	41.05° N	124.15° W	107	FM	Trinidad Head, CA, USA
UTA	CCGG	39.9° N	113.72° W	1320	FM	Wendover, Utah, USA
UUM	CCGG	44.45° N	111.1° E	914	FM	Ulaan Uul, Mongolia
WIS	CCGG	31.13° N	34.88° E	400	FM	Sede Boker, Israel
WLG	CCGG	36.27° N	100.92° E	3810	FM	Mt Waliguan, China
ZEP	CCGG	78.9° N	11.88° E	475	FM	Ny-Ålesund, Svalbard

Table 2. Comparison of different networks with NOAA CCGG at sites with parallel measurements. The mean difference is calculated as NOAA CCGG minus other (units of nmol mol^{-1}). The regression coefficient (slope) and intercept are given for a linear regression of the other network vs. NOAA CCGG.

Station	Network	Years compared	Mean difference	Regr. coeff.	Intercept
BRW	CATS	1998–2010	−0.52	0.976	8.08
NWR	CATS	2001–2010	−0.39	0.905	30.74
MLO	CATS	1999–2010	−0.20	1.022	−6.83
SMO	CATS	1999–2010	−0.59	0.966	11.49
SPO	CATS	1998–2010	−0.33	1.029	−8.90
RPB	AGAGE	1997–2010	−0.31	0.948	16.70
MHD	AGAGE	1997–2010	−0.44	0.960	13.30
SMO	AGAGE	1997–2010	−0.43	0.945	17.77
THD	AGAGE	2002–2010	−0.24	0.905	30.62
CGO	AGAGE	1997–2010	−0.55	0.958	13.77
ALT	CSIRO	1997–2010	−0.23	0.979	6.89
MLO	CSIRO	1997–2010	−0.1	1.041	−13.19
CGO	CSIRO	1997–2010	−0.31	0.984	5.48
SPO	CSIRO	1997–2010	−0.24	0.979	6.75

consistent with an assumed global total prior uncertainty of $2 \text{ Tg a}^{-1} \text{ N}$.

2.5.2 Observation error covariance matrix

Another key component of the Bayesian inversion is the observation uncertainty, which is described by the error covariance matrix, \mathbf{R} . A thorough description of the observation error variances is needed to avoid giving too strong weighting to very uncertain observations, which becomes particularly important if these observations are far from the expected value. The observation error variance takes into account the measurement and transport model errors. Measurement errors consist of random and systematic components. Random errors are assessed in determining the measurement reproducibility, while systematic errors, such as errors in the calibration, instrumentation, air sampling, etc., are more difficult to determine. For the measurement error, we have used the estimates given by the data providers, which includes random and, as far as is known, systematic errors and is approximately 0.3 ppb (circa 0.1%). For the transport model errors, we have estimated two contributions: (1) transport errors (following Rödenbeck et al., 2003) and (2) errors from a lack of subgrid-scale variability (following Bergamaschi et al., 2010), both of which were calculated using forward model simulations run with the same prior fluxes and meteorology as the inversions. The first error uses the 3-D mole fraction gradient around the grid cell where the site is located as a proxy for the transport error, and thus strong vertical and/or horizontal gradients lead to large error estimates. The second error uses the change in mole fraction in the grid cell integrated over the e-folding time for flushing the grid cell with the modelled wind speed. This is used as a proxy for the influence of not accounting for the homogeneous distribution

of fluxes within the grid cell and their location relative to the observation site (for details, see Bergamaschi et al. 2010). For observations from southern mid- to high-latitude sites, we have included an additional transport error to account for the fact that LMDz cannot accurately reproduce the seasonal cycle at these latitudes owing largely to errors in Southern Hemisphere stratosphere-to-troposphere transport. This is seen in a phase shift of the simulated vs. observed seasonal cycles of N_2O and CFC-12. Both these species have a stratospheric sink and tropospheric mixing ratios influenced by seasonal stratosphere-to-troposphere transport. This error was estimated to be approximately 1.0 ppb . We did not account for correlations between errors, i.e. \mathbf{R} is a diagonal matrix.

2.6 Forward model sensitivity tests

One major motivation of this study is to determine whether or not N_2O emissions vary interannually on a regional scale, driven, for example, by ENSO climate variability. Therefore, it is important to first ascertain whether such a flux signal can be detected by the current observational network. Since ENSO largely affects the tropics, in particular tropical and temperate South America, we focus on a hypothetical flux signal from this region. We performed forward model simulations to test the influence of low/high fluxes during 1 year in tropical and subtropical South America ($1 \text{ Tg a}^{-1} \text{ N}$ less/more evenly distributed over land than in the prior) on atmospheric N_2O mole fractions in an El Niño year (1998) and a La Niña year (1999), respectively. (The results of these tests are presented in Sect. 3.1.)

2.7 Inversion sensitivity tests

We ran five different inversion scenarios to test the robustness of the results to the observations used and to the inversion setup (see Table 4). Observation data contain gaps; in other words the data coverage is not consistent throughout the inversion period (see Fig. 2). Furthermore, some observation sites only became operational a few years after the start year of the inversion. The inconsistent data coverage over time results in varying degrees of constraint on the fluxes in space and time; therefore in periods with good data coverage, a stronger constraint on the fluxes is possible, whereas when there is poorer data coverage, the fluxes are closer to the prior. Hence, to examine interannual variations in the fluxes, it is necessary to distinguish between variations owing to inconsistent data coverage and those resulting from the atmospheric signal. Thus ran a set of inversions with as consistent as possible data coverage (the reference data set) and a set of inversions using all available observation sites. For the reference data set inversions, 15 sites were included, these having data throughout the inversion period and no gaps of longer than 6 months, while for the other inversions, 59 sites were included and no gap criterion was applied (see Table 1 for

Table 3. N₂O sources used in the a priori fluxes (totals shown for 2005).

Source type	Data set	Resolution	Total (Tg a ⁻¹ N)
terrestrial biosphere	ORCHIDEE O-CN	monthly	10.83
– agriculture (direct + indirect)			3.88
– natural soils			6.95
ocean	PISCES	monthly	4.28
waste water	EDGAR-4.1	annual	0.21
solid waste	EDGAR-4.1	annual	0.004
solvents	EDGAR-4.1	annual	0.05
fuel production	EDGAR-4.1	annual	0.003
ground transport	EDGAR-4.1	annual	0.18
industry combustion	EDGAR-4.1	annual	0.41
residential & other combustion	EDGAR-4.1	annual	0.18
shipping	EDGAR-4.1	annual	0.002
other sources	EDGAR-4.1	annual	0.0005
biomass burning	GFED-2.1	monthly	0.71
Total		monthly	16.84

Table 4. Overview of inversion sensitivity tests.

Test name	Prior fluxes	No. surface sites	No. observations	Measurement error
CLMR	climatology	15	144 849	0.3 ppb
I AVR	interannual	15	144 849	0.3 ppb
I AVA ^a	interannual	59	180 057	0.3 ppb
I AVE	interannual	59	180 057	0.5 ppb
I AVS ^b	interannual	59	180 057	0.3 ppb

^aIAVA is the control run. ^bI AVS is the same as the control run except that in this test the sink was also optimized.

the list of sites). The reference data set inversions also serve as a test for the influence of a potential NOAA CCGG scale shift (see Sect. 2.4) as only one NOAA CCGG site was included in this data set. The reference data set inversions consisted of one run using the interannually varying prior fluxes (I AVR) and one run with climatological prior fluxes (CLMR) to test the influence of the assumed flux interannual variability. For the CLMR run, 1 year of fluxes (2002) was repeated for every year. The other sets of inversions (using all data) were created with interannually varying fluxes and consisted of one run to test the sensitivity of the results to the observation error (I AVE), one test where the stratospheric sink was also included in the optimization (I AVS) according to the method described in Thompson et al. (2011), and a control run (I AVA) (see Table 4 for an overview of the sensitivity tests). (The results of these tests are presented in Sects. 3.2 and 3.3.)

2.8 Calculation of posterior flux errors

From the Lanczos algorithm used to find the gradient of $J(\mathbf{x})$, we also obtain an estimate of the leading eigenvectors of the Hessian matrix $J''(\mathbf{x})$. The number of eigenvectors obtained

equals the number of iterations performed. This fact is particularly useful since the inverse of $J''(\mathbf{x})$ gives the posterior flux error covariance matrix, \mathbf{A} . However, since the eigenvalues of $J''(\mathbf{x})$ are the reciprocals of the eigenvalues of \mathbf{A} , many iterations are needed to obtain sufficient eigenvalues and eigenvectors to approximate \mathbf{A} (Chevallier et al., 2005). Therefore, we use the Monte Carlo approach instead to estimate the posterior flux errors as described by Chevallier et al. (2007). In this approach, an ensemble of inversions is run with random perturbations in the prior fluxes and observations, consistent with \mathbf{B} and \mathbf{R} , respectively. The statistics of the ensemble of posterior fluxes are equivalent to the posterior uncertainty. For the uncertainty calculation we used an ensemble of 20 inversions of one year (2003) for the reference and full observation data sets. The prior and posterior uncertainties given in Table 5 are all calculated from the Monte Carlo ensemble.

3 Results

3.1 Robustness and uncertainty analysis

The current observational network has few sites in tropical regions and, notably, no sites in tropical and subtropical South America. However, some constraint on fluxes in this region is obtained from sites in the South Atlantic and equatorial Pacific. From the forward sensitivity tests, significant differences in atmospheric mole fractions at tropical and subtropical sites were found after 2–3 months and globally after circa 6 months following the perturbation. Figure 3 shows the difference in mole fraction (test scenario minus control run) at Samoa and Ascension Island for an El Niño year (low fluxes) and a La Niña year (high fluxes). The current measurement precision on a single flask sample

Table 5. Prior and posterior error ($\text{Tg a}^{-1} \text{N}$) and error reduction (ER) calculated from Monte Carlo ensembles for the reference data set (Ref) and all data (All).

Region	Error Prior	Error Ref	ER Ref %	Error All	ER All %
Global	2.17	0.62	71	0.52	76
North America	0.65	0.50	23	0.45	31
Tropical & South America	1.01	0.89	12	0.84	17
Europe	0.57	0.35	39	0.27	52
North Asia	0.30	0.30	0	0.27	10
South Asia	0.95	0.62	35	0.56	42
Africa	0.96	0.58	40	0.55	43
Australasia	0.26	0.25	3	0.25	4
Ocean 20–90° N	0.30	0.28	6	0.26	12
Ocean 20° S–20° N	0.61	0.51	17	0.48	21
Ocean 90–20° S	0.53	0.47	11	0.47	12

is approximately 0.3 ppb, so the signal after approximately 6 months (circa 0.2 ppb) will be detectable from the mean of 4 or more flask samples. If the change in flux persists for approximately 1 year, the atmospheric signal in the tropics reaches circa 0.3 ppb compared to 0.15 ppb in the extratropics, for example at Mace Head (53° N). Given that the magnitude of this signal is similar at all tropical and subtropical sites, the observational network would be sensitive to a regional change in fluxes of this magnitude in the tropics.

Figure 4 shows the annual mean error reduction per grid cell calculated as 1 minus the ratio of the posterior to prior flux error, where the posterior error is found from the Monte Carlo ensemble of inversions, for the reference and full observation data sets. As expected, the distribution of error reduction is strongly dependent on the observational network, with most of the reductions in the temperate northern latitudes. Despite the low error reduction at the grid-cell level in the tropics and Southern Hemisphere, modest error reductions are achieved by integrating the fluxes over regions. Table 5 shows the prior and posterior errors, and error reduction globally and for eight land and three ocean regions. Using all observations, strong error reductions were found for Europe (52%), North America (31%), South Asia (42%) and Africa (43%), while only moderate error reductions were found for South America (17%), North Asia (10%) and Australasia (4%). The error reductions using only the reference sites were somewhat smaller, notably so for Europe, North America and South Asia, where new observation sites were established during the inversion period.

3.2 Mean spatial distribution

The mean spatial distribution (1999–2009) of the posterior fluxes did not differ significantly between sensitivity tests, nor did the general distribution of the fluxes change remarkably throughout the 11-year period. For this reason, only the mean flux from the control inversion, IAVA, is shown (Fig. 5). Tropical and subtropical regions exhibited

the highest N_2O fluxes, in particular tropical and subtropical South America ($13 \pm 4\%$ of global total), South and East Asia ($20 \pm 3\%$), and tropical and subtropical Africa ($19 \pm 3\%$) (Table 6). High fluxes were also found for Europe ($6 \pm 1\%$), mostly in central Europe, and temperate North America ($7 \pm 2\%$), predominantly in the eastern states. This distribution is not unexpected, and a similar pattern is also seen in the prior fluxes. All inversions, however, increased the flux relative to the prior in South and East Asia, and to a lesser extent in tropical Africa, North America, tropical South America and southern Europe (Fig. 6). In contrast, the inversions slightly reduced the mean flux in southern Africa, southern South America, and in the Great Lakes region of North America.

Emissions from India and eastern China were found to be considerably more important than predicted in the prior. This may be due to an underestimate of mineral nitrogen fertilizer application rates. These rates having been increasing rapidly in recent years; however, in the prior model the fertilizer rates from 2006 to 2009 were based on 2005 statistics, and thus agricultural emissions in latter years may be underestimated in the prior. Another contributing factor may be an underestimate of reactive nitrogen deposition rates; for instance, deposition rates of NO_y (an important denitrification substrate) are known to be systematically underestimated in India (Dentener et al., 2006). In general, both India and China have very high rates of NO_3 (HNO_3 and nitrate aerosol) and NH_4^+ and NH_3 deposition, which has likely also increased in recent years owing to increased nitrogen fertilizer usage and industrial activities (Dentener et al., 2006). Emissions from tropical western Africa were also found to be more important than predicted in the prior, with flux levels comparable to those in eastern North America. This is somewhat surprising considering that the amount of mineral nitrogen fertilizer used in tropical Africa is only a small fraction of that used in North America (Potter et al., 2010). Although we cannot rule out the possibility that the inversion overestimates N_2O emissions in tropical Africa, due to, for example,

Table 6. Prior and posterior sources ($\text{Tg a}^{-1} \text{N}$) by region. Values are given as the mean over the period 1999 to 2009 and for the posterior source the results of the test IAVA are given.

Region	Prior	Prior %	Posterior	Posterior %
North America	1.14	6	1.32	7
Tropical & South America	2.62	15	2.53	13
Europe	1.06	6	1.25	6
North Asia	0.49	3	0.72	4
South Asia	3.11	17	3.79	20
Africa	3.44	19	3.53	19
Australasia	0.37	2	0.34	2
Ocean 20–90° N	1.18	7	1.29	7
Ocean 20° S–20° N	2.47	14	2.63	14
Ocean 90–20° S	1.92	11	1.58	8

atmospheric transport errors, there are reasons why the prior flux may be an underestimate. Statistics from this region are difficult to obtain, so there may be an under-reporting of fertilizer application rates. An additional factor is the supply of reactive nitrogen in the form of manure, for which the application rates are comparable to those in, for example, China (Potter et al., 2010). Manure application rates are not constrained by data in O-CN, and thus may be underestimated. Natural NO_y deposition in tropical regions, especially for tropical Africa and tropical Central and South America, is an important source of reactive nitrogen and may also be under-accounted for in O-CN (S. Zaehle, personal communication, 2012). Lastly, it is possible that the total soil emission in O-CN is underestimated for this region owing to the lack of a vertically resolved soil layer, which may result in errors in modelled soil moisture.

3.3 Temporal variability and trends

Over the 11-year period, the global total N_2O emission varied from 17.5 to 20.1 $\text{Tg a}^{-1} \text{N}$ (for the inversion IAVA) and the year-to-year variation was significantly higher (0.77 $\text{Tg a}^{-1} \text{N}$ 1 SD) than the variation between sensitivity tests for any given year (0.13 $\text{Tg a}^{-1} \text{N}$ mean SD) and the uncertainty of 0.5 $\text{Tg a}^{-1} \text{N}$ (Table 7). In contrast, there was little variability in the global total sink, which varied from 11.8 to 12.6 $\text{Tg a}^{-1} \text{N}$ (Table 8). The years 2002 and 2009 stood out as having particularly low emissions (17.5 and 18.1 $\text{Tg a}^{-1} \text{N}$, respectively), while in 2008 the emissions were the highest (20.1 $\text{Tg a}^{-1} \text{N}$).

In addition to variations in the N_2O source, the tropospheric mole fraction is influenced by variations in stratosphere-to-troposphere exchange (STE) as there is a strong gradient in N_2O mole fraction across the tropopause, and thus changes in the net air mass exchange between the stratosphere troposphere impact the tropospheric mole fraction (Nevison et al., 2007, 2011). Therefore, one important question that arises is, how sensitive are the inversion results to errors in the modelled STE? STE resulting in

Table 7. Global total source strength ($\text{Tg a}^{-1} \text{N}$) for each of the sensitivity tests.

Year	CLMR	I AVR	IAVA	IAVE	IAVS
1999	18.91	18.76	18.71	18.62	18.46
2000	19.29	19.25	19.41	19.34	19.31
2001	18.82	18.80	18.79	18.96	18.69
2002	17.72	17.70	17.45	17.46	17.24
2003	18.93	19.05	19.42	19.25	19.38
2004	18.93	18.90	18.96	19.06	18.84
2005	19.43	19.63	19.36	19.39	19.23
2006	19.73	19.71	19.91	19.75	19.80
2007	19.30	19.25	19.19	19.41	19.05
2008	20.06	20.30	20.10	20.07	19.90
2009	18.02	17.97	18.08	18.11	18.04

Table 8. Global sink strength ($\text{Tg a}^{-1} \text{N}$) for each of the sensitivity tests.

Year	CLMR	I AVR	IAVA	IAVE	IAVS
1999	12.21	12.22	12.22	12.22	12.09
2000	12.20	12.20	12.20	12.20	12.08
2001	12.07	12.07	12.07	12.07	11.97
2002	11.95	11.95	11.95	11.95	11.84
2003	12.12	12.12	12.12	12.12	12.02
2004	11.81	11.81	11.81	11.81	11.68
2005	12.04	12.04	12.04	12.04	11.92
2006	12.25	12.24	12.25	12.25	12.12
2007	12.53	12.53	12.53	12.53	12.42
2008	12.44	12.44	12.44	12.44	12.34
2009	12.63	12.63	12.63	12.63	12.53

non-reversible transport of air masses to the troposphere is to a large extent driven by the Brewer–Dobson circulation (Holton et al., 1995). We have found that the seasonality of STE in the Northern Hemisphere is reasonably well resolved by LMDz and there is good agreement between modelled and observed seasonal cycles for CFC-12, which has seasonality

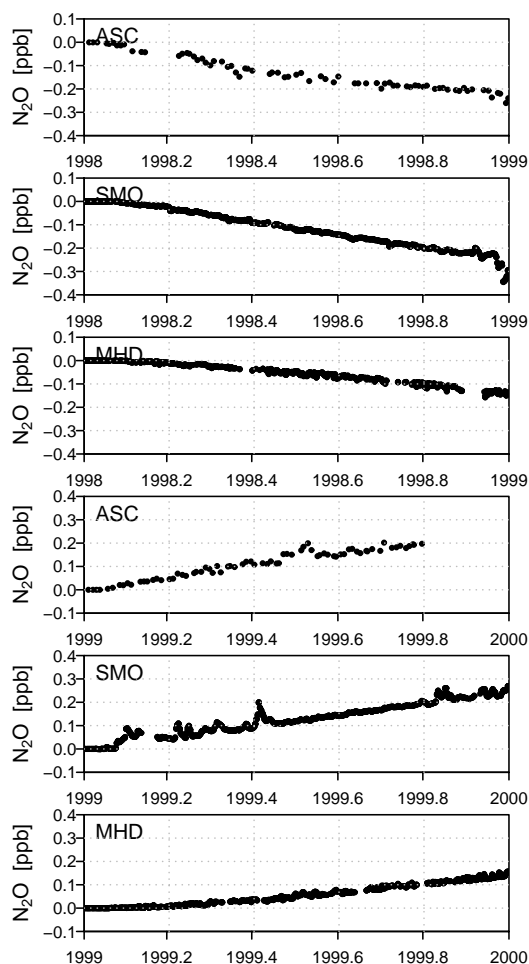


Fig. 3. Difference in mole fraction at Ascension Island (ASC, NOAA CCGG), America Samoa (SMO, AGAGE) and Mace Head (MHD, AGAGE) for the case of low vs. control fluxes in tropical South America and South America for an El Niño year (upper three panels) and for the case of high vs. control fluxes for a La Niña year (lower three panels). Model simulation has been sampled according to the available observations at these sites.

strongly dependent on STE. The agreement is poorer for the Southern Hemisphere, and here the error in the observation space was increased to account for this. Interannual variability in STE appears to be also reasonably well captured by LMDz, again based on comparisons of CFC-12 observed and modelled interannual variations ($R = 0.57$ for the period 1996–2009) (Thompson et al., 2013).

To examine the possible drivers of the interannual variability in the N_2O source, and to look at regional trends, the fluxes were aggregated into eight different geographic and climatic regions and three ocean regions (see Figs. 7 and 8). Figure 7 shows the prior and posterior annual flux anomalies integrated over each land region. Generally, the results for all sensitivity tests were in close agreement with one another. The fact that the test using a flux climatology as the prior

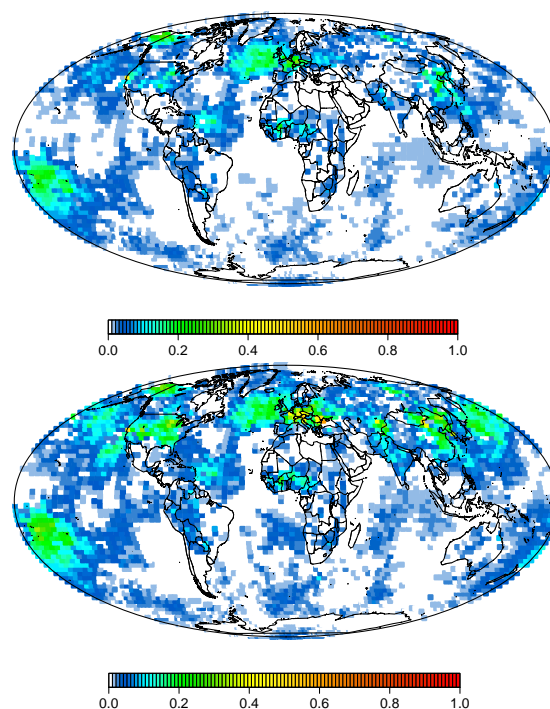


Fig. 4. Annual mean (for 2003) error reduction (shown as a fraction of 1) for the reference data set (upper panel) and the full data set (lower panel).

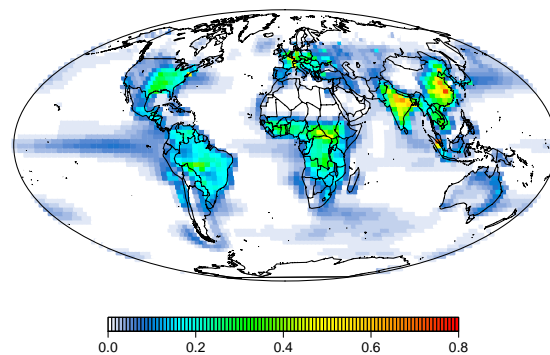


Fig. 5. Mean N_2O flux (upper panel) and standard deviation (lower panel) for the period 1999–2009 shown for IAVA (units of $g\ m^{-2}\ a^{-1}\ N$).

(CLMR, orange) was close to the results using interannually varying prior fluxes provides confidence that the year-to-year variations are largely driven by the atmospheric observations. Furthermore, there is good agreement between the results from the tests using the reference vs. the full observation data set, indicating that a few sites are sufficient to capture flux interannual variability at (sub)-continental scales.

At the global scale, a weak positive trend in the N_2O source was found ($0.05\ Tg\ a^{-2}\ N$) but was not significant at the 95 % confidence level (p value of 0.5). The only statistically significant trend was found in South Asia, where the

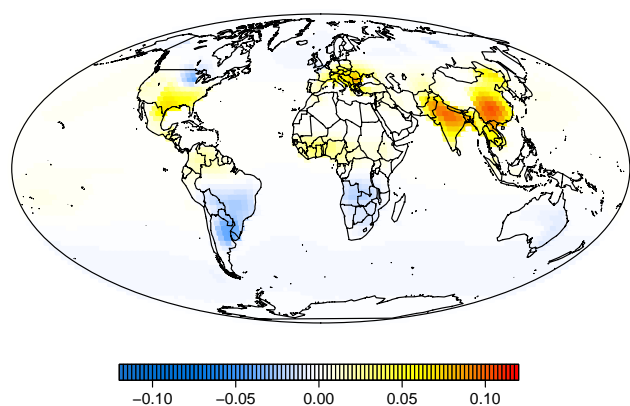


Fig. 6. Mean N_2O flux increments (a posteriori minus a priori fluxes) for the period 1999–2009 shown for IAVA (units of $\text{g m}^{-2} \text{a}^{-1} \text{N}$).

source increased at a rate of $0.045 \text{ Tg a}^{-2} \text{N}$ (median of all sensitivity tests, p value of 0.006) between 1999 and 2009 (see Fig. 7). Although a similar trend ($0.049 \text{ Tg a}^{-2} \text{N}$) is seen in the prior fluxes, this signal is not only driven by the prior, as the test CLMR also shows a similar trend.

4 Discussion

4.1 Emission trends in South Asia

The economies of South Asia, in particular those of China and India, have undergone rapid growth in the past decade. This has been seen in increased industrialization and energy consumption. It has also led to a growing demand for food and thus an expansion and intensification of agriculture.

According to the Food and Agricultural Organization of the United Nations (FAO) statistics, nitrogen fertilizer consumption in China has increased on average by $0.66 \text{ Tg a}^{-1} \text{N}$ between 2002 and 2010 (<http://www.fao.org/corp/statistics/en/>). During the same period, the total harvested area for all crops increased by 51 Mha, leading to further increases in agricultural emissions. As a simple approximation, using a 1.25% emission factor for direct agricultural emissions, as recommended by the IPCC (Mosier et al., 1998), would lead to an increase of $0.008 \text{ Tg a}^{-2} \text{N}$. These calculations do not account for indirect N_2O emissions associated with nitrogen leaching and atmospheric transport of reactive nitrogen, which lead to increased N_2O emissions in areas distant from where the fertilizer was applied. A more complete estimate of the increase in agricultural emissions, which also includes indirect emissions, is given by the EDGAR-4.2 inventory: on average $0.026 \text{ Tg a}^{-2} \text{N}$ between 2000 and 2008. Increased energy consumption in China has also led to greater N_2O emission, contributing $0.009 \text{ Tg a}^{-2} \text{N}$ and emissions from chemical production and solvent use contributing a further $0.002 \text{ Tg a}^{-2} \text{N}$ (EDGAR-4.2). In total (i.e. across all sec-

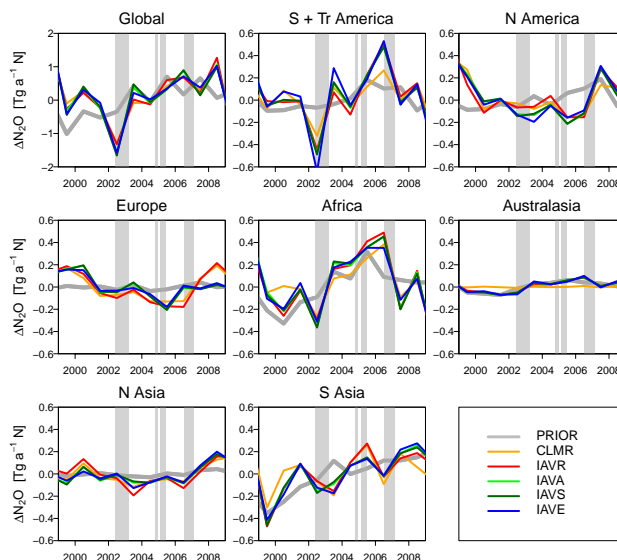


Fig. 7. Global and land regions annual flux anomalies (units of $\text{Tg a}^{-1} \text{N}$). The grey-shaded areas indicate El Niño events ($\text{MEI} \geq 0.6$).

tors), EDGAR-4.2 estimates that Chinese N_2O emissions have been increasing at an average rate of $0.042 \text{ Tg a}^{-2} \text{N}$ (from 2000 to 2008).

In India, a similar trend in nitrogen fertilizer consumption is seen with an average increase of $0.68 \text{ Tg a}^{-1} \text{N}$ from 2002 to 2010 (FAO). In contrast to China, however, there has been negligible change in crop area. Furthermore, despite the strong increase in nitrogen fertilizer use, EDGAR-4.2 does not estimate a large change in agricultural emissions of N_2O (only $0.005 \text{ Tg a}^{-2} \text{N}$), nor does it in the total emissions (only $0.0075 \text{ Tg a}^{-2} \text{N}$), for 2000 to 2008. It is beyond the scope of this study to speculate as to why there is an apparent discrepancy between the FAO statistics and the EDGAR-4.2 estimate for agricultural emissions. However, it is noteworthy that the average change in total emissions for China and India (approximately $0.05 \text{ Tg a}^{-2} \text{N}$) is in close agreement to that found for South Asia by the inversions ($0.045 \text{ Tg a}^{-2} \text{N}$).

4.2 Interannual variability in fluxes

4.2.1 Tropical and subtropical land

The largest interannual variations in N_2O emissions are seen in the tropical and subtropical land regions, i.e. tropical South America and South America, and Africa. In Fig. 7, periods with a multivariate ENSO index (MEI, <http://www.esrl.noaa.gov/psd/enso/mei/>) value above 0.6, i.e. El Niño events, have been shaded in grey. El Niño events occurred from mid-2002 to 2003 and in 2007, with weak El Niño conditions between 2004 and 2006. The El Niño events of 2002 and 2007 coincide with negative N_2O flux anomalies, while La Niña conditions generally coincide

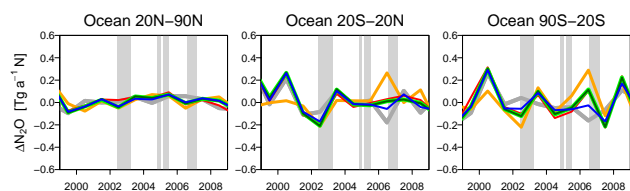


Fig. 8. Ocean region flux anomalies (units of $\text{Tg a}^{-1} \text{N}$). The grey-shaded areas indicate El Niño events ($\text{MEI} \geq 0.6$). (Legend the same as in Fig. 7.)

with positive N_2O flux anomalies. (Unfortunately, there are insufficient accurate N_2O measurements available prior to the late 1990s to resolve regional fluxes; hence, it is not possible to study the period of the strong El Niño of 1997–1998.) Since our atmospheric transport model is nudged to ERA-interim wind fields (see Sect. 2.2), the effects of inter-annual variations in transport are accounted for. Therefore, it is unlikely that the correlation of the emissions with MEI is an artefact of ENSO-related atmospheric transport changes.

ENSO has a well-known climate impact in tropical and subtropical South America, Asia, Australia and southern Africa (Trenberth et al., 1998, and references therein) and may be driving the changes in N_2O land flux, as proposed by Thompson et al. (2013), Ishijima et al. (2009) and Saikawa et al. (2013). The strongest climate effects generally occur from December to February, and during an El Niño event these bring warm and dry conditions to the central and eastern parts of South America, southern Africa and tropical and subtropical Asia. La Niña, on the other hand, is associated with cooler and wetter conditions in these regions. To investigate a possible link between climate and N_2O flux, we analysed precipitation, soil moisture and temperature data from ECMWF ERA-Interim (Dee et al., 2011) at 80 km resolution. These meteorological parameters are known to strongly influence the rates of denitrification and nitrification and to modulate N_2O flux at the local scale (Davidson, 1993; Smith et al., 1998). It is, however, beyond this scope of this study to fully analyse the sensitivity of N_2O emissions to climate, which in itself is an ambitious, albeit important, research topic. In this study, we only discuss correlations between meteorological anomalies and N_2O fluxes and their possible causes.

The strong negative N_2O flux anomaly in 2002 corresponds with negative precipitation and soil moisture anomalies over tropical and subtropical South America and Africa (see Fig. 10), in areas with significant mean N_2O flux (i.e. in areas with a mean soil N_2O flux above $0.1 \text{ g m}^{-2} \text{ a}^{-1} \text{ N}$ according to the prior flux estimate). Differences in N_2O soil fluxes between, for example, the El Niño year 2002 and the near-neutral year 2003 can be seen over Brazil and central Africa, where the flux is lower in 2002 (Fig. 9).

However, not all negative precipitation and soil moisture anomalies are associated with low N_2O flux and vice versa. The severity of the water deficiency may be important in

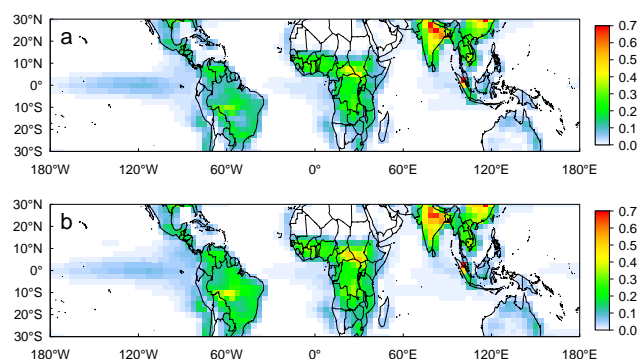


Fig. 9. Annual mean N_2O flux ($\text{g m}^{-2} \text{ a}^{-1} \text{ N}$) from the inversion IAVA, shown for the tropics in the El Niño year 2002 (a) and the near-neutral year 2003 (b).

determining whether or not N_2O production in soils is affected. N_2O flux peaks in soils with between 50 and 80 % or 60 and 90 % water-filled pore space (WFPS), depending on soil type, and drops off exponentially below this threshold (Bouwman, 1998). Therefore, the water limitation would need to be severe enough to make a significant change in WFPS. A severe drought could potentially also affect the availability of reactive nitrogen in unfertilized regions by slowing the rate of mineralization of organic matter in soils (Borken and Matzner, 2009). An important link between soil moisture, mineralization rates and N_2O flux in tropical soils on seasonal timescales has already been proposed by Potter et al. (1996), and may also be important on interannual timescales. Furthermore, using a data-calibrated biogeochemical model, Werner et al. (2007) found significant interannual variability in the tropical rainforest soil N_2O source, which was largely driven by changes in rainfall. For example, for African rainforests the N_2O source was found to change by $0.21 \text{ Tg a}^{-1} \text{ N}$ (50 %) from 1993 to 1994 (Werner et al., 2007), a magnitude commensurate with the standard deviation of emissions from Africa in the inversions ($0.3 \text{ Tg a}^{-1} \text{ N}$). In tropical and subtropical South America, the standard deviation of the emissions from the inversions is close to that for Africa ($0.26 \text{ Tg a}^{-1} \text{ N}$), and represents about 10 % of the total mean flux of this region.

4.2.2 Temperate land

Interannual variations in temperate N_2O soil fluxes, i.e. in North America, North Asia and Europe, are smaller than those found in the tropics. In North America, low N_2O flux is found for 2005–2006 and coincides with negative precipitation and soil moisture anomalies in the ECMWF ERA-Interim data (Dee et al., 2011) (see Fig. 10). In 2007, higher N_2O fluxes are found and coincide with the return of precipitation rates to average values. High fluxes are also seen in 1999, and coincide with a positive soil temperature anomaly and a weak positive anomaly in soil moisture. In Europe, low

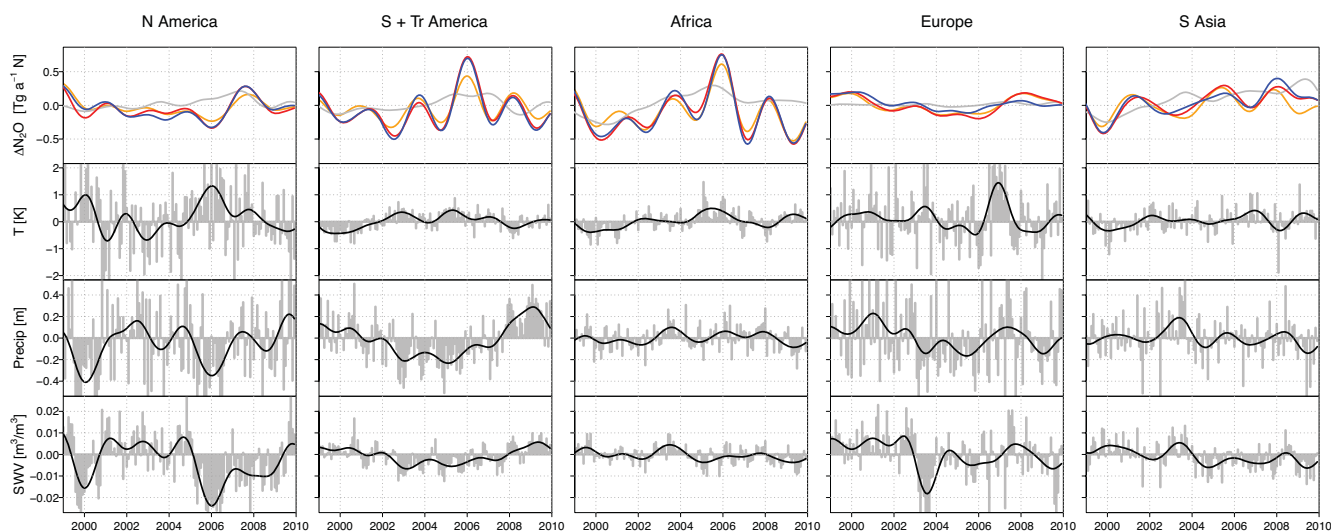


Fig. 10. Comparisons of the interannual variability in N_2O flux with anomalies in soil temperature (T), precipitation (Precip) and soil water volume (SWV) (ECMWF ERA-Interim). For the fluxes, the legend is the same as in Fig. 7. For the meteorological variables, the grey bars indicate the monthly anomaly and the solid line the interannual variability.

N_2O flux is seen in 2005 and corresponds to a small negative anomaly in temperature, soil moisture and precipitation (see Fig. 10). Although significant negative anomalies in precipitation and soil moisture also occurred in 2003, no anomaly was seen in the annual total flux for this year. However, the flux interannual variability (calculated from the monthly fluxes using a Butterworth filter to remove seasonal variations) shows a negative flux anomaly of about $0.2 \text{ Tg a}^{-1} \text{ N}$ in the second half of 2003 and a positive anomaly of similar magnitude in the first half of the year, which cancel out in the annual total.

4.2.3 Ocean

Considerable interannual variability in N_2O flux is also seen in the tropical (20° N to 20° S) and southern oceans (20° S to 90° S) (Fig. 8). In general, low N_2O flux coincides with El Niño, in 2002 and 2007, and high N_2O flux with La Niña, in 2000, 2006 and 2008. The inversion results are fairly consistent for all sensitivity tests. One notable exception is in the year 2006, where in the tropical ocean the inversion CLMR (using a climatological prior) stands out with a strong positive anomaly, which is not seen in the other inversions for which the interannually varying prior was used. This discrepancy may be a result of too few degrees of freedom for the flux to depart from the prior N_2O flux estimate, which is too low in the interannually varying fluxes.

ENSO has a strong influence on ocean upwelling and thus on air–sea gas exchange. During El Niño, warm water in the western Pacific migrates eastward and reduces upwelling in the eastern Pacific off the coast of South America, while during La Niña the process is reversed and there is an increase in upwelling (McPhaden et al., 2006). Changes in upwelling af-

fect air–sea N_2O fluxes through physical and biological processes: physically, by changing the supply of N_2O -rich water from below the euphotic zone to the surface and thereby the partial pressure of N_2O in the surface water, and biologically, by changing the supply of nutrients to the surface layer and thus primary production and the production of N_2O within the surface layer (Nevison et al., 2007). These processes are parameterized in the biogeochemistry model PISCES, used for the prior ocean N_2O flux in the inversion (Dutreuil et al., 2009). PISCES was coupled to a climate model and is thus sensitive to ENSO driven changes. However, as the climate model was unconstrained, the variability does not necessarily reflect the real timing of ENSO. The atmospheric inversion helps constrain the timing of the ENSO driven changes in ocean N_2O flux and verifies the magnitude of these changes, which are of the order of $0.4 \text{ Tg a}^{-1} \text{ N}$ globally.

5 Summary and conclusions

We present estimates of N_2O fluxes from 1999 to 2009 based on the inversion of atmospheric transport and observations of atmospheric N_2O mole fractions. To determine the sensitivity of the inversion results to the coverage of the observations, the prior fluxes used, the strength of the stratospheric sink and the assigned observation error, five different inversion tests were carried out. All five inversions produced consistent results within the posterior error margin, which indicates a fair representation of the prior errors in the inversion system. Over the 11 years period, the global total N_2O source varied from 17.5 to $20.1 \text{ Tg a}^{-1} \text{ N}$ (control inversion, IAVA), with a SD of $0.77 \text{ Tg a}^{-1} \text{ N}$. The year-to-year variability in the global source was significantly larger than the variability

between inversions in any given year ($0.13 \text{ Tg a}^{-1} \text{ N}$ mean SD). Tropical and subtropical land regions were found to have the highest N_2O emissions; in particular, South Asia (20% of global total), tropical South America and South America (13%) and Africa (19%), while the temperate regions of Europe (6%) and North America (7%) were less important. A global trend in the N_2O source of $0.05 \text{ Tg a}^{-2} \text{ N}$ was detected but was not significant at the 95% confidence level. The only significant trend in N_2O emissions was in the region of South Asia ($0.045 \text{ Tg a}^{-2} \text{ N}$) and is consistent with inventory estimates from EDGAR-4.2. This trend appears to be primarily driven by increasing agricultural emissions (about 60% of the trend) and secondarily by increased energy consumption (about 20%). Interannual variability in the global N_2O source was largely driven by variability in tropical and subtropical soil fluxes, in particular in tropical South America and South America ($0.3 \text{ Tg a}^{-1} \text{ N}$ 1 SD) and to a lesser extent in Africa ($0.3 \text{ Tg a}^{-1} \text{ N}$ 1 SD). Significant variability was also found in N_2O fluxes in the tropical and southern oceans (0.15 and $0.2 \text{ Tg a}^{-1} \text{ N}$ 1 SD, respectively). We found a strong correlation of N_2O flux interannual variability with ENSO, where El Niño conditions are associated with lower N_2O fluxes and vice versa for La Niña. The mechanism for the ENSO– N_2O relationship is most likely through climate changes in tropical and subtropical South America and Africa affecting soil N_2O fluxes and through changes in upwelling in the eastern Pacific affecting the ocean N_2O flux. ENSO-driven changes in the land and ocean fluxes are in the same direction and thus reinforce the change in the tropospheric N_2O mole fraction. These results show that the tropospheric N_2O mole fraction is sensitive to climate-driven changes in soil and ocean N_2O fluxes. Furthermore, the climate-driven interannual variability in the global N_2O source (of the order of $1 \text{ Tg a}^{-1} \text{ N}$) is an order of magnitude larger than the average annual increase in the source over the period 1999–2009, indicating that climate is a significant factor in modulating the global annual source of N_2O .

Acknowledgements. We are very grateful for the input and feedback from S. Zaehle, L. Bopp and W. Lahoz. We thank G. van der Werf for use of the GFED data and the EDGAR team for the use of their inventory data. We also acknowledge the support of the LSCE computing services. This work was jointly financed by the European Commission under the EU Seventh Research Framework Programme (grant agreement no. 283576. MACC-II) and by the Norwegian Research Council (contract no. 193774, SOGG-EA).

Edited by: J. Kaiser

References

- Bergamaschi, P., Krol, M., Meirink, J. F., Dentener, F., Segers, A., van Aardenne, J., Monni, S., Vermeulen, A. T., Schmidt, M., Ramonet, M., Yver, C., Meinhardt, F., Nisbet, E. G., Fisher, R. E., O'Doherty, S., and Dlugokencky, E. J.: Inverse modeling of European CH_4 emissions 2001–2006, *J. Geophys. Res.*, 115, D22309, doi:10.1029/2010jd014180, 2010.
- Borken, W. and Matzner, E.: Reappraisal of drying and wetting effects on C and N mineralization and fluxes in soils, *Glob. Change Biol.*, 15, 808–824, 2009.
- Bousquet, P., Peylin, P., Ciais, P., Le Quééré, C., Friedlingstein, P., and Tans, P. P.: Regional Changes in Carbon Dioxide Fluxes of Land and Oceans Since 1980, *Science*, 290, 1342–1346, 2000.
- Bousquet, P., Ciais, P., Miller, J. B., Dlugokencky, E. J., Hauglustaine, D. A., Prigent, C., Van der Werf, G. R., Peylin, P., Brunke, E. G., Carouge, C., Langenfelds, R. L., Lathière, J., Papa, F., Ramonet, M., Schmidt, M., Steele, L. P., Tyler, S. C., and White, J.: Contribution of anthropogenic and natural sources to atmospheric methane variability, *Nature*, 443, 439–443, 2006.
- Bouwman, A. F.: Environmental science: Nitrogen oxides and tropical agriculture, *Nature*, 392, 866–867, 1998.
- Bouwman, A. F., Boumans, L. J. M., and Batjes, N. H.: Modeling global annual N_2O and NO emissions from fertilized fields, *Global Biogeochem. Cy.*, 16, 1080, doi:10.1029/2001GB001812, 2002.
- Chen, Y.-H. and Prinn, R. G.: Estimation of atmospheric methane emissions between 1996 and 2001 using a three-dimensional global chemical transport model, *J. Geophys. Res.-Atmos.*, 111, D10307, doi:10.1029/2005JD006058, 2006.
- Chevallier, F., Fisher, M., Peylin, P., Serrar, S., Bousquet, P., Bréon, F.-M., Chédin, A., and Ciais, P.: Inferring CO_2 sources and sinks from satellite observations: Method and application to TOVS data, *J. Geophys. Res.*, 110, D24309, doi:10.1029/2005JD006390, 2005.
- Chevallier, F., Bréon, F.-M., and Rayner, P. J.: Contribution of the Orbiting Carbon Observatory to the estimation of CO_2 sources and sinks: Theoretical study in a variational data assimilation framework, *J. Geophys. Res.*, 112, D09307, doi:10.1029/2006JD007375, 2007.
- Corazza, M., Bergamaschi, P., Vermeulen, A. T., Aalto, T., Haszpra, L., Meinhardt, F., O'Doherty, S., Thompson, R., Moncrieff, J., Popa, E., Steinbacher, M., Jordan, A., Dlugokencky, E., Brühl, C., Krol, M., and Dentener, F.: Inverse modelling of European N_2O emissions: assimilating observations from different networks, *Atmos. Chem. Phys.*, 11, 2381–2398, doi:10.5194/acp-11-2381-2011, 2011.
- Crutzen, P. J., Mosier, A. R., Smith, K. A., and Winiwarter, W.: N_2O release from agro-biofuel production negates global warming reduction by replacing fossil fuels, *Atmos. Chem. Phys.*, 8, 389–395, doi:10.5194/acp-8-389-2008, 2008.
- Davidson, E. A.: Soil water content and the ratio of nitrous to nitric oxide emitted from soil, *Biogeochemistry of global change: Radiatively active trace gases*, edited by: Oremland, R. S., Chapman and Hall, London, 369–386, 1993.
- Dee, D. P., Uppala, S. M., Simmons, A. J., Berrisford, P., Poli, P., Kobayashi, S., Andrae, U., Balmaseda, M. A., Balsamo, G., Bauer, P., Bechtold, P., Beljaars, A. C. M., van de Berg, L., Bidlot, J., Bormann, N., Delsol, C., Dragani, R., Fuentes, M., Geer, A. J., Haimberger, L., Healy, S. B., Hersbach, H., Hólm, E. V., Isaksen, I., Kållberg, P., Köhler, M., Matricardi, M., McNally, A. P., Monge-Sanz, B. M., Morcrette, J. J., Park, B. K., Peubey, C., de Rosnay, P., Tavolato, C., Thépaut, J. N., and Vitart, F.: The ERA-Interim reanalysis: configuration and performance of the

- data assimilation system, *Q. J. Roy. Meteor. Soc.*, 137, 553–597, 2011.
- Denman, K. L., Brasseur, G. P., Chidthaisong, A., Ciais, P., Cox, P. M., Dickinson, R. E., Hauglustaine, D., Heinze, C., Holland, E., Jacob, D., Lohmann, U., Ramachandran, S., da Silva Dias, P. L., Wofsy, S. C., and Zhang, X.: Couplings Between Changes in the Climate System and Biogeochemistry, *Climate Change 2007: The Physical Science Basis, Contribution of Working Group I to the Fourth Assessment Report of the Intergovernmental Panel on Climate Change*, edited by: Solomon, S. D., Qin, D., Manning, M., Chen, Z., Marquis, M., Averyt, K. B., Tignor, M., and Miller, H. L., Cambridge University Press, Cambridge, 499–587, 2007.
- Dentener, F., Drevet, J., Lamarque, J. F., Bey, I., Eickhout, B., Fiore, A. M., Hauglustaine, D., Horowitz, L. W., Krol, M., Kulshreshtha, U. C., Lawrence, M., Galy-Lacaux, C., Rast, S., Shindell, D., Stevenson, D., Van Noije, T., Atherton, C., Bell, N., Bergman, D., Butler, T., Cofala, J., Collins, B., Doherty, R., Ellingsen, K., Galloway, J., Gauss, M., Montanaro, V., Müller, J. F., Pitari, G., Rodriguez, J., Sanderson, M., Solmon, F., Strahan, S., Schultz, M., Sudo, K., Szopa, S., and Wild, O.: Nitrogen and sulfur deposition on regional and global scales: A multimodel evaluation, *Global Biogeochem. Cy.*, 20, GB4003, doi:10.1029/2005gb002672, 2006.
- Dutreuil, S., Bopp, L., and Tagliabue, A.: Impact of enhanced vertical mixing on marine biogeochemistry: lessons for geo-engineering and natural variability, *Biogeosciences*, 6, 901–912, doi:10.5194/bg-6-901-2009, 2009.
- Errico, R. M.: What is an Adjoint Model?, *B. Am. Meteorol. Soc.*, 78, 2577–2591, 1997.
- Forster, P., Ramaswamy, V., Artaxo, P., Berntsen, T., Betts, R., Fahey, D. W., Haywood, J., Lean, J., Lowe, D. C., Myhre, G., Nganga, J., Prinn, R., Raga, G., Schultz, M., and Van Dorland, R.: Changes in Atmospheric Constituents and in Radiative Forcing, *Climate Change 2007: The Physical Science Basis, Contribution of Working Group I to the Fourth Assessment Report of the Intergovernmental Panel on Climate Change*, edited by: Solomon, S., Qin, D., Manning, M., Chen, Z., Marquis, M., Averyt, K. B., Tignor, M., and Miller, H. L., Cambridge University Press, Cambridge, United Kingdom, 2007.
- Francey, R. J., Steele, L. P., Spencer, D. A., Langenfelds, R. L., Law, R. M., Krümmel, P. B., Fraser, P. J., Etheridge, D. M., Derek, N., Coram, S. A., Cooper, L. N., Allison, C. E., Porter, L., and Baly, S.: The CSIRO (Australia) measurement of greenhouse gases in the global atmosphere Baseline Atmospheric Program Australia 1999–2000, Melbourne, Australia, Bureau of Meteorology and CSIRO Atmospheric Research, 42–53, 2003.
- Hall, B. D., Dutton, G. S., and Elkins, J. W.: The NOAA nitrous oxide standard scale for atmospheric observations, *J. Geophys. Res.*, 112, D09305, doi:10.1029/2006jd007954, 2007.
- Hauglustaine, D. A., Hourdin, F., Jourdain, L., Filiberti, M.-A., Walters, S., Lamarque, J.-F., and Holland, E. A.: Interactive chemistry in the Laboratoire de Météorologie Dynamique general circulation model: Description and background tropospheric chemistry evaluation, *J. Geophys. Res.*, 109, D04314, doi:10.1029/2003JD003957, 2004.
- Hirsch, A. I., Michalak, A. M., Bruhwiler, L. M., Peters, W., Dlugokencky, E. J., and Tans, P. P.: Inverse modeling estimates of the global nitrous oxide surface flux from 1998–2001, *Global Biogeochem. Cy.*, 20, GB1008, doi:10.1029/2004gb002443, 2006.
- Holton, J. R., Haynes, P. H., McIntyre, M. E., Douglass, A. R., Rood, R. B., and Pfister, L.: Stratosphere-troposphere exchange, *Rev. Geophys.*, 33, 403–439, 1995.
- Hourdin, F. and Armengaud, A.: The Use of Finite-Volume Methods for Atmospheric Advection of Trace Species. Part I: Test of Various Formulations in a General Circulation Model, *Mon. Weather Rev.*, 127, 822–837, 1999.
- Hourdin, F., Musat, I., Bony, S., Braconnot, P., Codron, F., Dufresne, J.-L., Fairhead, L., Filiberti, M.-A., Friedlingstein, P., Grandpeix, J.-Y., Krinner, G., Le Van, P., Li, Z.-X., and Lott, F.: The LMDZ4 general circulation model: climate performance and sensitivity to parameterized physics with emphasis on tropical convection, *Clim. Dynam.*, 27, 787–813, 2006.
- Huang, J., Golombek, A., Prinn, R., Weiss, R., Fraser, P., Simmonds, P., Dlugokencky, E. J., Hall, B., Elkins, J., Steele, P., Langenfelds, R., Krümmel, P., Dutton, P., and Porter, L.: Estimation of regional emissions of nitrous oxide from 1997 to 2005 using multinetwork measurements, a chemical transport model, and an inverse method, *J. Geophys. Res.*, 113, D17313, doi:10.1029/2007JD009381, 2008.
- Ishijima, K., Nakazawa, T., and Aoki, S.: Variations of atmospheric nitrous oxide concentration in the northern and western Pacific, *Tellus B*, 61, 408–415, 2009.
- Lanczos, C.: An iteration method for the solution of the eigenvalue problem, *J. Res. Nat. Bur. Stand.*, 45, 255–282, 1950.
- McPhaden, M. J., Zebiak, S. E., and Glantz, M. H.: ENSO as an Integrating Concept in Earth Science, *Science*, 314, 1740–1745, 2006.
- Mellor, G. L. and Yamada, T.: Development of a Turbulence Closure Model for Geophysical Fluid Problems, *Rev. Geophys. Space Ge.*, 20, 851–875, 1982.
- Minschwaner, K., Salawitch, R. J., and McElroy, M. B.: Absorption of Solar Radiation by O₂: Implications for O₃ and Lifetimes of N₂O, CFCl₃, and CF₂Cl₂, *J. Geophys. Res.*, 98, 10543–10561, 1993.
- Mosier, A., Kroeze, C., Nevison, C., Oenema, O., Seitzinger, S., and van Cleemput, O.: Closing the global N₂O budget: nitrous oxide emissions through the agricultural nitrogen cycle, *Nutr. Cycl. Agroecosys.*, 52, 225–248, 1998.
- Nevison, C. D., Mahowald, N. M., Weiss, R. F., and Prinn, R. G.: Interannual and seasonal variability in atmospheric N₂O, *Global Biogeochem. Cy.*, 21, GB3017, doi:10.1029/2006gb002755, 2007.
- Nevison, C. D., Dlugokencky, E., Dutton, G., Elkins, J. W., Fraser, P., Hall, B., Krümmel, P. B., Langenfelds, R. L., O'Doherty, S., Prinn, R. G., Steele, L. P., and Weiss, R. F.: Exploring causes of interannual variability in the seasonal cycles of tropospheric nitrous oxide, *Atmos. Chem. Phys.*, 11, 3713–3730, doi:10.5194/acp-11-3713-2011, 2011.
- Peylin, P., Bousquet, P., Le Quééré, C., Sitch, S., Friedlingstein, P., McKinley, G. A., Gruber, N., Rayner, P., and Ciais, P.: Multiple constraints on regional CO₂ flux variations over land and oceans, *Global Biogeochem. Cy.*, 19, GB1011, doi:10.1029/2003gb002214, 2005.
- Potter, P., Ramankutty, N., Bennett, E. M., and Donner, S. D.: Characterizing the Spatial Patterns of Global Fertilizer Application and Manure Production, *Earth Interact.*, 14, 1–22, 2010.

- Potter, C. S., Matson, P. A., Vitousek, P. M., and Davidson, E. A.: Process modeling of controls on nitrogen trace gas emissions from soils worldwide, *J. Geophys. Res.*, 101, 1361–1377, 1996.
- Prather, M. J., Holmes, C. D., and Hsu, J.: Reactive greenhouse gas scenarios: Systematic exploration of uncertainties and the role of atmospheric chemistry, *Geophys. Res. Lett.*, 39, L09803, doi:10.1029/2012GL051440, 2012.
- Prinn, R. G., Weiss, R. F., Fraser, P. J., Simmonds, P. G., Cunnold, D. M., Alyea, F. N., O'Doherty, S., Salameh, P., Miller, B. R., Huang, J., Wang, R. H. J., Hartley, D. E., Harth, C., Steele, L. P., Sturrock, G., Midgley, P. M., and McCulloch, A.: A history of chemically and radiatively important gases in air deduced from ALE/GAGE/AGAGE, *J. Geophys. Res.*, 105, 17751–17792, 2000.
- Ravishankara, A. R., Daniel, J. S., and Portmann, R. W.: Nitrous Oxide (N₂O): The Dominant Ozone-Depleting Substance Emitted in the 21st Century, *Science*, 326, 123–125, 2009.
- Rayner, P. J., Enting, I. G., Francey, R. J., and Langenfelds, R.: Reconstructing the recent carbon cycle from atmospheric CO₂, δ¹³C and O₂/N₂ observations, *Tellus B*, 51, 213–232, 1999.
- Rödenbeck, C., Houweling, S., Gloor, M., and Heimann, M.: CO₂ flux history 1982–2001 inferred from atmospheric data using a global inversion of atmospheric transport, *Atmos. Chem. Phys.*, 3, 1919–1964, doi:10.5194/acp-3-1919-2003, 2003.
- Saikawa, E., Schlosser, C. A., and Prinn, R. G.: Global modeling of soil nitrous oxide emissions from natural processes, *Global Biogeochem. Cy.*, 27, 927–989, 2013.
- Skiba, U. and Smith, K. A.: The control of nitrous oxide emissions from agricultural and natural soils, *Chemosphere – Global Change Science*, 2, 379–386, 2000.
- Smith, K. A., Thomson, P. E., Clayton, H., McTaggart, I. P., and Conen, F.: Effects of temperature, water content and nitrogen fertilisation on emissions of nitrous oxide by soils, *Atmos. Environ.*, 32, 3301–3309, 1998.
- Syakila, A. and Kroeze, C.: The global nitrous oxide budget revisited, *Greenhouse Gas Measurement and Management*, 1, 17–26, 2011.
- Thompson, R. L., Bousquet, P., Chevallier, F., Rayner, P. J., and Ciais, P.: Impact of the atmospheric sink and vertical mixing on nitrous oxide fluxes estimated using inversion methods, *J. Geophys. Res.*, 116, D17307, doi:10.1029/2011jd015815, 2011.
- Thompson, R. L., Dlugokenky, E., Chevallier, F., Ciais, P., Dutton, G., Elkins, J. W., Langenfelds, R. L., Prinn, R. G., Weiss, R. F., Tohjima, Y., Krummel, P. B., Fraser, P., and Steele, L. P.: Interannual variability in tropospheric nitrous oxide, *Geophys. Res. Lett.*, 40, 4426–4431, 2013.
- Tiedtke, M.: A comprehensive mass flux scheme for cumulus parameterization in large-scale models, *Mon. Weather Rev.*, 117, 1779–1800, 1989.
- Tohjima, Y., Mukai, H., Maksyutov, S., Takahashi, Y., Machida, T., Katsumoto, M., and Fujinuma, Y.: Variations in atmospheric nitrous oxide observed at Hateruma monitoring station, *Chemosphere – Global Change Science*, 2, 435–443, 2000.
- Trenberth, K. E., Branstator, G. W., Karoly, D., Kumar, A., Lau, N.-C., and Ropelewski, C.: Progress during TOGA in understanding and modeling global teleconnections associated with tropical sea surface temperatures, *J. Geophys. Res.*, 103, 14291–14324, 1998.
- Uppala, S. M., Koallberg, P. W., Simmons, A. J., Andrae, U., Bechtold, V. D. C., Fiorino, M., Gibson, J. K., Haseler, J., Hernandez, A., Kelly, G., Li, X., Onogi, K., Saarinen, S., Sokka, N., Allan, R. P., Andersson, E., Arpe, K., Balmaseda, M. A., Beljaars, A. C. M., van de Berg, L., Bidlot, J., Bormann, N., Caires, S., Chevallier, F., Dethof, A., Dragosavac, M., Fisher, M., Fuentes, M., Hagemann, S., Hölm, E., Hoskins, B. J., Isaksen, I., Janssen, P. A. E. M., Jenne, R., McNally, A. P., Mahfouf, J.-F., Morcrette, J.-J., Rayner, N. A., Saunders, R. W., Simon, P., Sterl, A., Trenberth, K. E., Untch, A., Vasiljevic, D., Viterbo, P., and Woollen, J.: The ERA-40 Reanalysis, *Q. J. Roy. Meteorol. Soc.*, 131, 2961–3012, 2005.
- van der Werf, G. R., Randerson, J. T., Giglio, L., Collatz, G. J., Mu, M., Kasibhatla, P. S., Morton, D. C., DeFries, R. S., Jin, Y., and van Leeuwen, T. T.: Global fire emissions and the contribution of deforestation, savanna, forest, agricultural, and peat fires (1997–2009), *Atmos. Chem. Phys.*, 10, 11707–11735, doi:10.5194/acp-10-11707-2010, 2010.
- Van Leer, B.: Towards the ultimate conservative difference scheme. Part IV: A new approach to numerical convection, *J. Comput. Phys.*, 23, 276–299, 1977.
- Volk, C. M., Elkins, J. W., Fahey, D. W., Dutton, G. S., Gilligan, J. M., Loewenstein, M., Podolske, J. R., Chan, K. R., and Gunson, M. R.: Evaluation of source gas lifetimes from stratospheric observations, *J. Geophys. Res.*, 102, 25543–525564, 1997.
- Werner, C., Butterbach-Bahl, K., Haas, E., Hickler, T., and Kiese, R.: A global inventory of N₂O emissions from tropical rainforest soils using a detailed biogeochemical model, *Global Biogeochem. Cy.*, 21, GB3010, doi:10.1029/2006gb002909, 2007.
- WMO: Greenhouse Gas Bulletin: The State of Greenhouse Gases in the Atmosphere Based on Global Observations through 2010, Atmospheric Environment Research Division, Research Department, World Meteorological Organisation, Geneva, 2011.
- Xu, R., Prentice, I. C., Spahni, R., and Niu, H. S.: Modelling terrestrial nitrous oxide emissions and implications for climate feedback, *New Phytol.*, 196, 472–488, 2012.
- Zaehle, S. and Friend, A. D.: Carbon and nitrogen cycle dynamics in the O-CN land surface model: 1. Model description, site-scale evaluation, and sensitivity to parameter estimates, *Global Biogeochem. Cy.*, 24, GB1005, doi:10.1029/2009gb003521, 2010.
- Zaehle, S., Friend, A. D., Friedlingstein, P., Dentener, F., Peylin, P., and Schulz, M.: Carbon and nitrogen cycle dynamics in the O-CN land surface model: 2. Role of the nitrogen cycle in the historical terrestrial carbon balance, *Global Biogeochem. Cy.*, 24, GB1006, doi:10.1029/2009gb003522, 2010.
- Zaehle, S., Ciais, P., Friend, A. D., and Prieur, V.: Carbon benefits of anthropogenic reactive nitrogen offset by nitrous oxide emissions, *Nat. Geosci.*, 4, 601–605, 2011.